Article

Not peer-reviewed version

Mirror-Image RNA: A Right-Handed Z-Form RNA and Its Ligand Complex

Yi Song , Shiyu Wang , Yan Xu *

Posted Date: 8 October 2024

doi: 10.20944/preprints202410.0457.v1

Keywords: mirror-image; right-hand; Z-form L-RNA; RNA-ligand complex

 doi:10.20944/preprints202410.0457.v1

Article

Mirror-Image RNA: A Right-Handed Z-Form RNA and Its Ligand Complex

Yi Song †, Shiyu Wang † and Yan Xu *

Division of Chemistry, Department of Medical Sciences, Faculty of Medicine, University of Miyazaki, 5200 Kihara, Kiyotake, Miyazaki 889-1692, Japan

* Correspondence: xuyan@med.miyazaki-u.ac.jp; Tel.: +81-985-85-0993

† These authors contributed equally to this work.

Abstract: Until now, Z-form RNAs were believed to only adopt a left-handed double helix structure. In this study, we describe the first observation of a right-handed Z-form RNA in NMR solution formed by L-nucleic acid RNA and present the first resolution structure of the complex between a right-handed Z-form RNA and a curaxin ligand. These results provide a platform for the design of topology specific Z-form-targeting compounds and is valuable for the development of new potent anticancer drugs.

Keywords: mirror-image; right-hand; Z-form L-RNA; RNA-ligand complex

1. Introduction

Nucleic acids have exquisitely evolved to store genetic information, primarily composed of D-nucleic acids, folding into the most common secondary structure with right-handed double-helical conformational features, fundamentally recognized as A-RNA or B-DNA (Scheme 1 left column). The right-handed A-form RNA plays a crucial role in cellular processes and functions such as responding to viral infections, post-transcriptional gene silencing, RNA silencing, and RNA interference [1-6].

A mirror-image of native D-nucleic acids, L-nucleic acids in a left-handed A-form (Scheme 1 left column), offers superior stability in biological environments due to their resistance to cellular nucleases [7,8]. The unique folding scaffold that L-RNA consisting of is used to recognize a variety of small molecules, peptides, and proteins [9,10]. Several aptamers are now under clinical investigation [11]. Simultaneously, chimeras of L-oligonucleotide containing nanotechnology materials are employed for drug delivery by enhancing stability [12].

The left-handed Z-form double helix structure, including Z-RNA and Z-DNA, has been shown to play an important role in multiple physiological events, including the regulation of gene expression, nucleosome positioning, and genetic instability associated with nucleic acid damage and repair (Scheme 1 right column) [13-16]. We recently suggested the relationship between Z-form structure and several diseases, such as cancer and inflammation [3,13,14,17,18]. Double-stranded Z-RNA consists of nucleotides arranged in a pattern where the nucleobases alternate between *syn*/*anti* conformations [19]. For the typical purine/pyrimidine repeats, cytidine residues indicate the *anti* conformation, while guanosine residues display the *syn* conformation, and the phosphate backbone follows a zig-zag course in discontinuous manner [20,21]. Some Cchemical modifications favor the *syn* conformation of guanosine, leading to stabilized Z-form [22]. We have demonstrated that trifluoromethyl introduction at the C8 position of guanosine, with the least energetic level, allowed guanosine to adopt the *syn* conformation to stabilize the Z-form [23].

Tremendous efforts have been devoted to identifying small molecules for interacting with Z-form. For instance, metal molecules recognize Z-form DNA structures, and our previous report showed that (P)-Helicene displays chiral selection in binding to Z-DNA [24]. We recently identified a small molecule, curaxin CBL0137, which promotes the Z-form transition of DNA and RNA in the nucleus [17]. This transition activates protein Z-DNA-binding protein 1 (ZBP1)-mediated apoptosis and necroptosis, contributing to its antitumor effects.

 doi:10.20944/preprints202410.0457.v1

While Z-form nucleic acid duplexes have been widely studied, all reported structures consistently adopt a left-handed helix. This gap in our understanding motivated us to explore whether a mirror-image, right-handed Z-form nucleic acid could exist and what unique topological features it might present. Such a discovery holds the potential to reveal new biological and medical functions, especially in understanding how nucleic acid molecules fold into complex, high-order structures and participate in vital processes and pathogenesis. Furthermore, studying the interactions between right-handed Z-form RNA and ligands could facilitate the development of novel nucleic acid-based nanomaterials, which have promising applications in drug delivery and targeted therapies. Herein, we present the first NMR structure of right-handed Z-form RNA in solution and investigate its interaction with curaxin ligand, CBL0137.

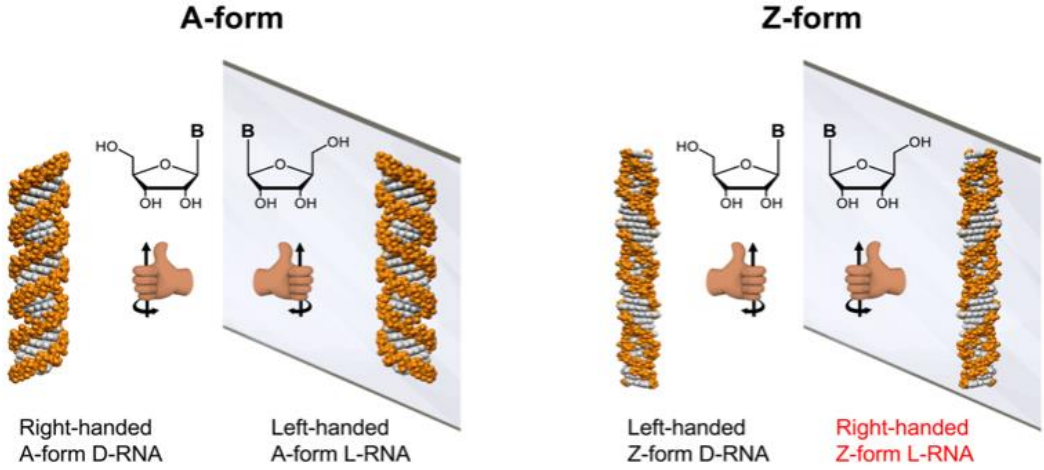

Scheme 1. Illustration of mirror-image RNA. The left column displays a right-handed helix A-form D-RNA and its mirror-image, a left-handed A-form L-RNA consisting of L-nucleic acids. The right column shows the left-handed helix Z-form D-RNA and its mirror-image with, a right-handed Z-form L-RNA consisting of L-nucleic acids.

2. Results

2.1. Synthesis of Right-Handed Z-form RNA and Characterization by CD and ^{19}F NMR

To uncover the structural features of right-handed Z-form RNA, we designed and synthesized a novel 8-^{F}G-modified L-guanosine analog (^{F}G), in which a trifluoromethyl (CF_3) group is introduced into the C8 position of L-guanosine according to previously reported method, and incorporated it into an RNA sequence L-r(CGC^{F}GCG)$_2$ (Figure 1 and Supplemental Data S1-S20) [25]. As reported in our previous research, a CF_3 group at the C8 position greatly stabilizes the Z-form nucleic acids and acts as a ^{19}F sensor, which can be used to study DNA and RNA structures using ^{19}F NMR [23]. We used circular dichroism spectroscopy (CD) to monitor the conformational state at various $NaClO_4$ concentrations. We observed that L-r(CGC^{F}GCG)$_2$ greatly stabilized the Z-RNA, showing the A–Z transition in the presence of only 50 mM $NaClO_4$ (Figure 2a), while the transition requires 6000 mM $NaClO_4$ for unmodified L-r(CGCGCG)$_2$ (Figure 2b). The result is completely consistent with ^{19}F NMR, which has been successfully used to distinguish RNA structures in our previous studies (Figure 2c) [26]. In ^{19}F NMR, a strong-intensity peak appeared as Z-form (−61.32 ppm) accompanied by a small peak (−60.20 ppm) at a $NaClO_4$ concentration of 100 mM, indicating the major Z-form RNA and a minor A-form RNA. With increasing $NaClO_4$ concentration, only the peak of Z-form RNA remained with strong intensity, whereas the peak of the A-form completely disappeared.

CD spectroscopy was performed to distinguish the RNA mirror enantiomer. The right-handed A-form D-r(CGCGCG)$_2$ exhibited a negative band around 290 nm and a positive band at 266 nm, which are typical A-form signals (Figure 2d). A left-handed A-form L-r(CGCGCG)$_2$ as the enantiomer was completely antithetical. Meanwhile, the right-handed Z-form RNA L-r(CGC^{F}GCG)$_2$ and the left-handed Z-form RNA D-r(CGC^{F}GCG)$_2$ stabilized by CF_3-modified D-guanosine showed absolutely mirror-imaged spectral signals (Figure 2e).

Preprints.org (www.preprints.org) | NOT PEER-REVIEWED | Posted: 8 October 2024 doi:10.20944/preprints202410.0457.v1

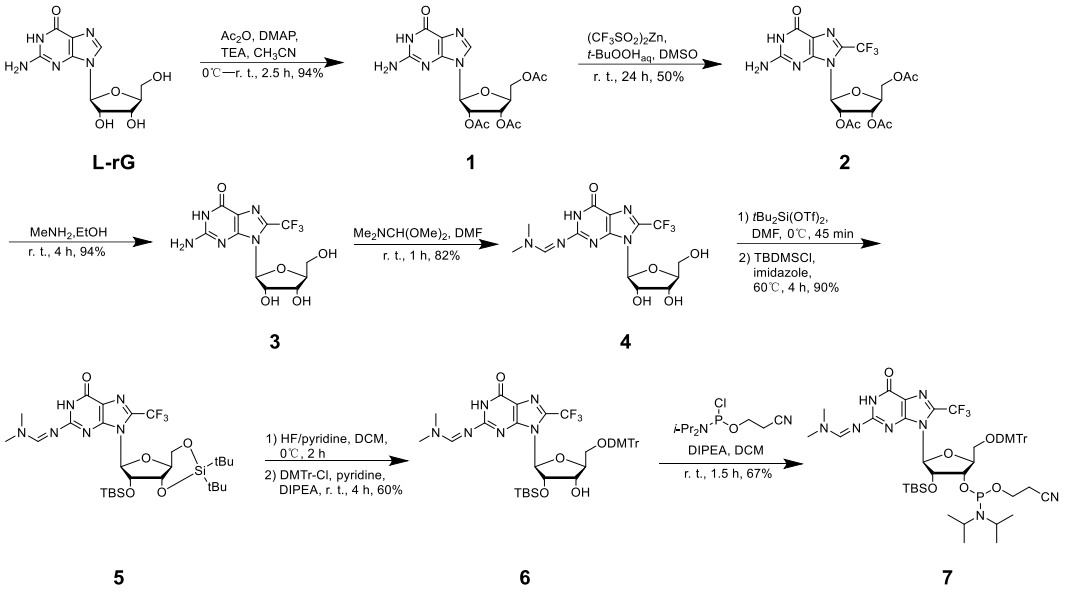

Figure 1. Synthetic scheme of ^{F}G and relative phosphoramidite compound.

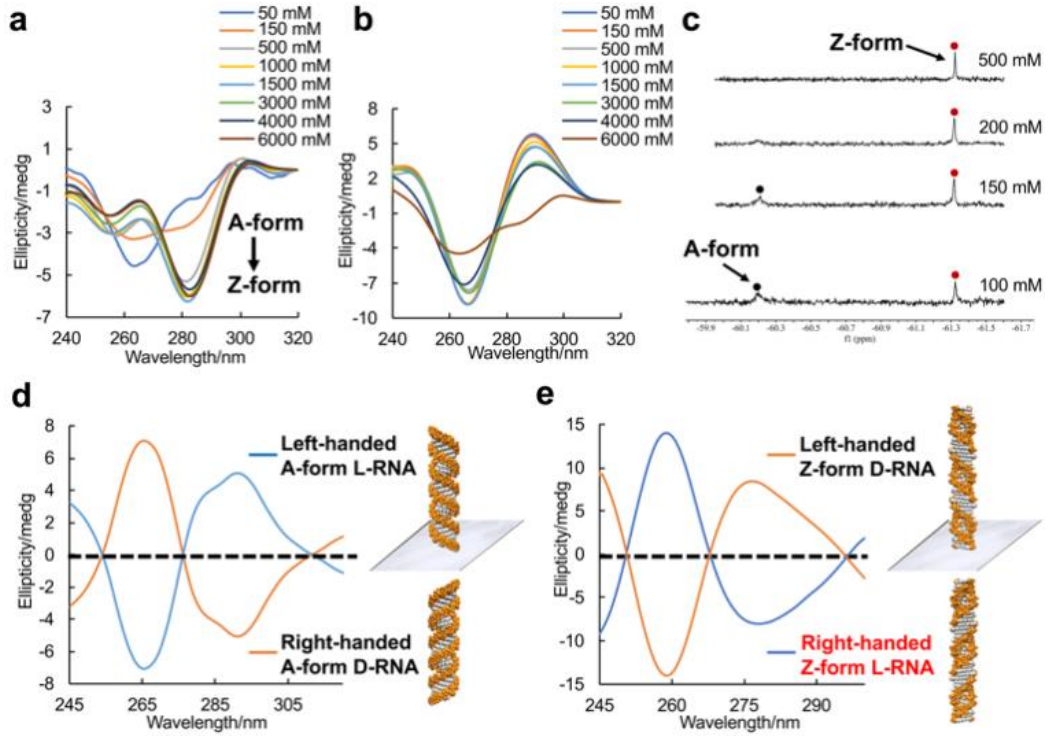

Figure 2. Enantiomers of A-form and Z-form RNA duplex structures. (a) CD spectra of the A–Z transition of L-RNA r(CGC^{F}GCG)$_2$ at various $NaClO_4$ concentrations at 10 °C. A negative Cotton effect appears around 285 nm with increasing $NaClO_4$ concentration. (b) CD spectra of L-RNA r(CGCGCG)$_2$ at various $NaClO_4$ concentrations at 10 °C. (c) ^{19}F NMR spectra of L-RNA r(CGC^{F}GCG)$_2$ in 5 mM Na-PO_4 buffer (pH 7.0) and various $NaClO_4$ concentrations. Red and black spots indicated Z-form and A-form RNA, respectively. (d) CD spectra of A-form RNA mirror enantiomers: left-handed L-RNA r(CGCGCG)$_2$ and right-handed D-RNA r(CGCGCG)$_2$ in presence of 5 mM Na-PO_4 buffer (pH 7.0) and 1.5 M $NaClO_4$ at 10 °C. (e) CD spectra of Z-form RNA mirror enantiomers: left-handed D-RNA r(CGC^{F}GCG)$_2$ and right-handed L-RNA r(CGC^{F}GCG)$_2$ in presence of 5 mM Na-PO_4 buffer (pH 7.0) and 1.5 M $NaClO_4$ at 10 °C.

2.2. NMR Solution Structure of Right-Handed Z-Form RNA

 doi:10.20944/preprints202410.0457.v1

To reveal the detailed structure of right-handed Z-form RNA, we performed the 2D NMR experiments (Figure 3). A complete list of ^{1}H chemical shifts was shown in Supplemental Table S1. The NOE-restrained refinement provided an unequivocal demonstration that the structure of L-RNA r(CGC^{F}GCG)$_2$ is Z-RNA. Sequential assignments of C_1 to C_3 and C_5 to G_6 for the Z-form can complete the pathway: C_1(H6/H5″)-G_2(H8/H1′)-C_3(H6/H5″), C_5(H6/H5″)-G_6(H8/H1′) (Figure 3a,c,d), indicating a sequence-specific connectivity for right-handed helices. All H5′′ of cytidine were found to shift upfield by 2.85 (C_1), 2.70 (C_3) and 2.66 (C_5) ppm, these alterations only could be observed in Z-form nucleic acid duplex (Figure 3a). The clear cross-peaks of the imino proton of $^{F}G_4$ (~13.48 ppm) and G_2 (~13.36 ppm) with the amino proton of C_3 (~6.49 ppm) and C_5 (~8.74 ppm) collectively suggested Watson–Crick base pairs (Figure 3b). Moreover, the H8/H1′ cross-peak region of the 2D NOESY spectrum showed only strong intranucleotide G_2(H8/H1′) and G_6(H8/H1′) cross-peaks (Figure 3c), which indicated the *syn* conformation of rG residues. Strong intra-residue cross peaks of C_1(H6/H5′′), C_3(H6/H5′′) and C_5(H6/H5′′) indicate *anti*-conformation of all cytidines in Z-form (Figure 3a). We note that the C_1H5 proton has cross-peaks to the C_5 amino proton (C_1H5/C_5NH2$_2$), and the C_5H5 proton has cross-peaks to the C_1 amino proton (C_5H5/ C_1NH2$_2$) (Figure 3d). Such cross-peaks can only happen between the two interstrand cytosines between C_1 in one strand and C_5 in another strand of the Z-RNA because of their specific base pair stacking pattern. Additionally, the NOE G_2H3′/G_2H4′ was observed and indicated that rG residues preserve the C3′-*endo* sugar pucker while those signals including C_1H1′/C_1H2′, C_3H1′/C_3H2′ and C_5H1′/C_5H2′, demonstrated rC residues in C2′-*endo* sugar pucker (Supplemental Figure S1).

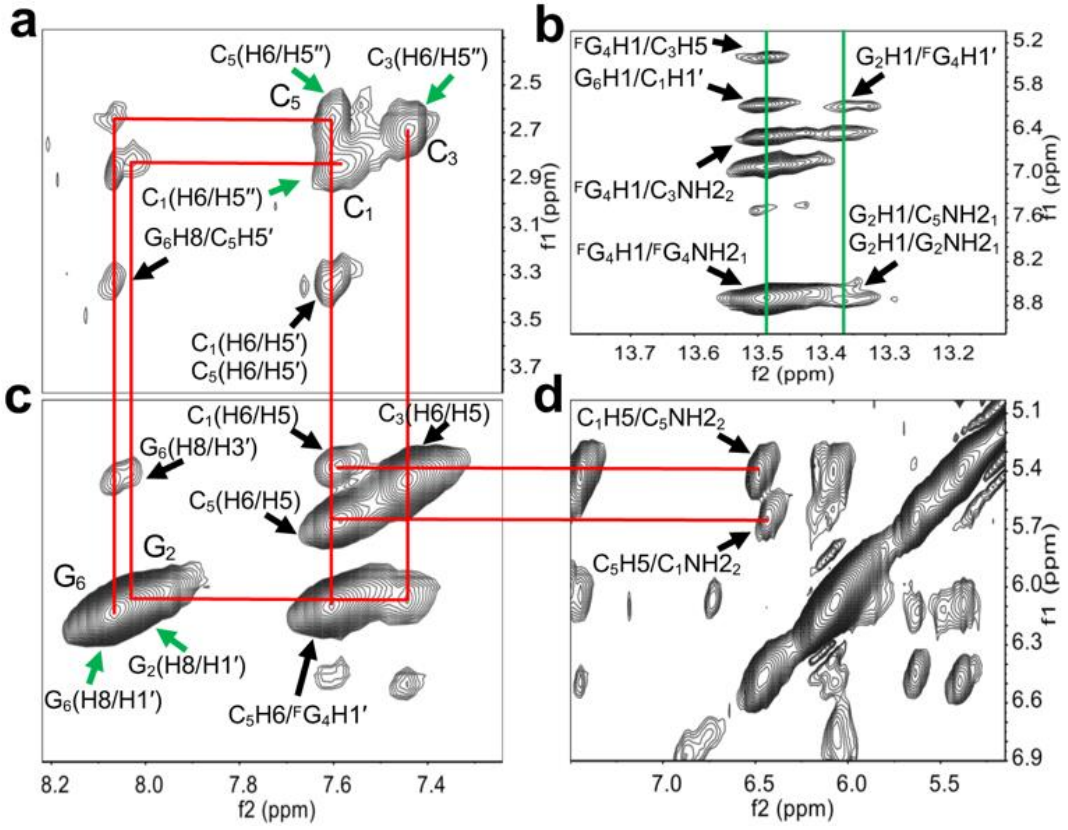

Figure 3. Structural determination of right-handed Z-form RNA r($C_1G_2C_3{}^{F}G_4C_5G_6$)$_2$. (a), (c) and (d) show wide-ranging connectivity path (red lines) [C_1(H6/H5″)-G_2(H8/H1′)-C_3(H6/H5″), C_5(H6/H5″)-G_6(H8/H1′)] in RNA strand of right-handed Z-helices in contour plot of the 2D-NOESY spectrum. (a) C_1(H6/H5′′), C_3(H6/H5′′) and C_5(H6/H5′′) were found to upshift 2.85, 2.70, and 2.66 ppm (green arrows). Strong intra-residue cross peaks of C_1(H6/H5′′), C_3(H6/H5′′) and C_5(H6/H5′′) were observed. Additional anomeric-aromatic proton interactions were assigned as C_1(H6/H5′), C_5(H6/H5′) and G_6H8/C_5H5′ marked by black arrows. (b) The cross peaks of imino proton of G_2 and amino proton of C_5, as well as imino proton of $^{F}G_4$ and amino proton of C_3 associated with G_6H1/C_1H1′, $^{F}G_4$H1/C_3H5, G_2H1/$^{F}G_4$H1′ were observed (green lines). Intraresidue NOE cross-peaks of imino and

 doi:10.20944/preprints202410.0457.v1

amino proton of G_2 and $^{F}G_4$ are shown. (c) Strong H8–H1′ cross peaks were observed (green arrows). C_1(H6/H5), C_3(H6/H5), C_5(H6/H5), G_6(H8/H3′), and C_5H6/$^{F}G_4$H1′ were labeled by black arrows. (d) The Z-RNA structural specific cross-peaks were observed between C_5 amino proton and C_1H5 as well as between C_1 amino proton and C_5H5 from inter-stranded interactions. These signals could be linked to C_1(H6/H5) and C_5(H6/H5) in (c) by red lines.

The structural model of L-r(CGC^{F}GCG)$_2$ is constructed based on the reported Z-form structure and NOE-constrained refining method (Supplemental Table S2). The molecular dynamics simulation was carried out in BIOVIA Discovery Studio 4.5 through a standard dynamic cascade with some modifications. The lowest energy conformation was selected as shown in Figure 4a and Supplemental Figure S2. The Watson–Crick scheme of base pairing is observed throughout the duplex, in which rG residues are characterized by a *syn* conformation in C3′-*endo* and rC with an *anti* conformation in C2′-*endo* (Figure 4b and Supplemental Figure S3 and S4). For the both CpG and GpC steps, base stacking interactions are observed but evidently no inter-strand base stacking (Figure 4c and Supplemental Figure S5), these results were in high agreement with the landmark of Z-helices.

To further clearly observe the right-handed Z-form RNA, we generated the model of a full-turn Z-RNA helix by excluding both terminal base pairs of the 6-mer structure (Figure 4d). The right-handed RNA helix has a well-marked zig-zag shape of the phosphorsugar backbone, exposed 2′-OH groups of rG to the outer helix surface (Figure 4d and Supplemental Figure S6). This might be considered as a result of the fact that the Z-RNA duplex structure requires higher salt concentration comparing to Z-DNA. Another feature of the RNA helix is that both grooves are well defined, possessing a very engraved, deep and much narrower minor groove, and a shallow major groove, which is the same as its mirror-image left-handed Z-form D-RNA (Supplemental Figure S6).

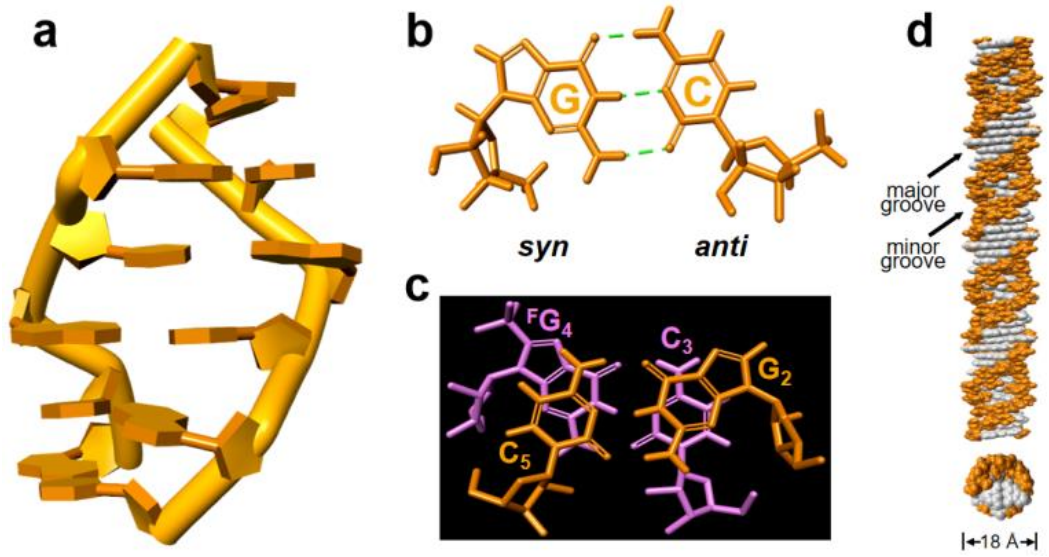

Figure 4. The structural model of right-handed Z-form RNA r($C_1G_2C_3{}^{F}G_4C_5G_6$)$_2$. (a) Structural right-handed Z-form RNA r(CGC^{F}GCG)$_2$ viewed from the major groove. (b) rG in *syn*-conformation and rC with *anti*-conformation form Watson–Crick base pair through three hydrogen bonds in Z-form RNA. (c) Stacking pattern within the GpC step in Z-RNA as viewed along the helix z-axis, showing only intra- but no inter-strand stacking. (d) An extending model of the right-handed Z-form RNA helix from Z-form RNA r(CGC^{F}GCG)$_2$ visualized in side (up) and top (bottom) views to show their base pair location and groove architecture, in which white represent base pairs and orange indicate phosphate-ribose backbones. The duplex diameter was shown, and the major or minor groove was indicated.

 doi:10.20944/preprints202410.0457.v1

2.3. Complex Structure of Right-Handed Z-Form RNA and Ligand CBL0137

We have identified a small molecule, the curaxin CBL0137 (Figure 5a), which is capable of inducing Z-form formation to activate ZBP1-mediated cell death. This encouraged us to explore its binding affinity with the right-handed Z-form RNA model of right-r(CGC^{F}GCG)$_2$. In CD spectroscopy, we observed the appearance of a negative band around 280 nm with the addition of equimolar (1:1) amounts of CBL0137 (Figure 5b). This effect was even more pronounced at a higher ratio (2:1) of CBL0137 to L-r(CGC^{F}GCG)$_2$. These results suggest that CBL0137 effectively converts the A-RNA conformation to Z-RNA.

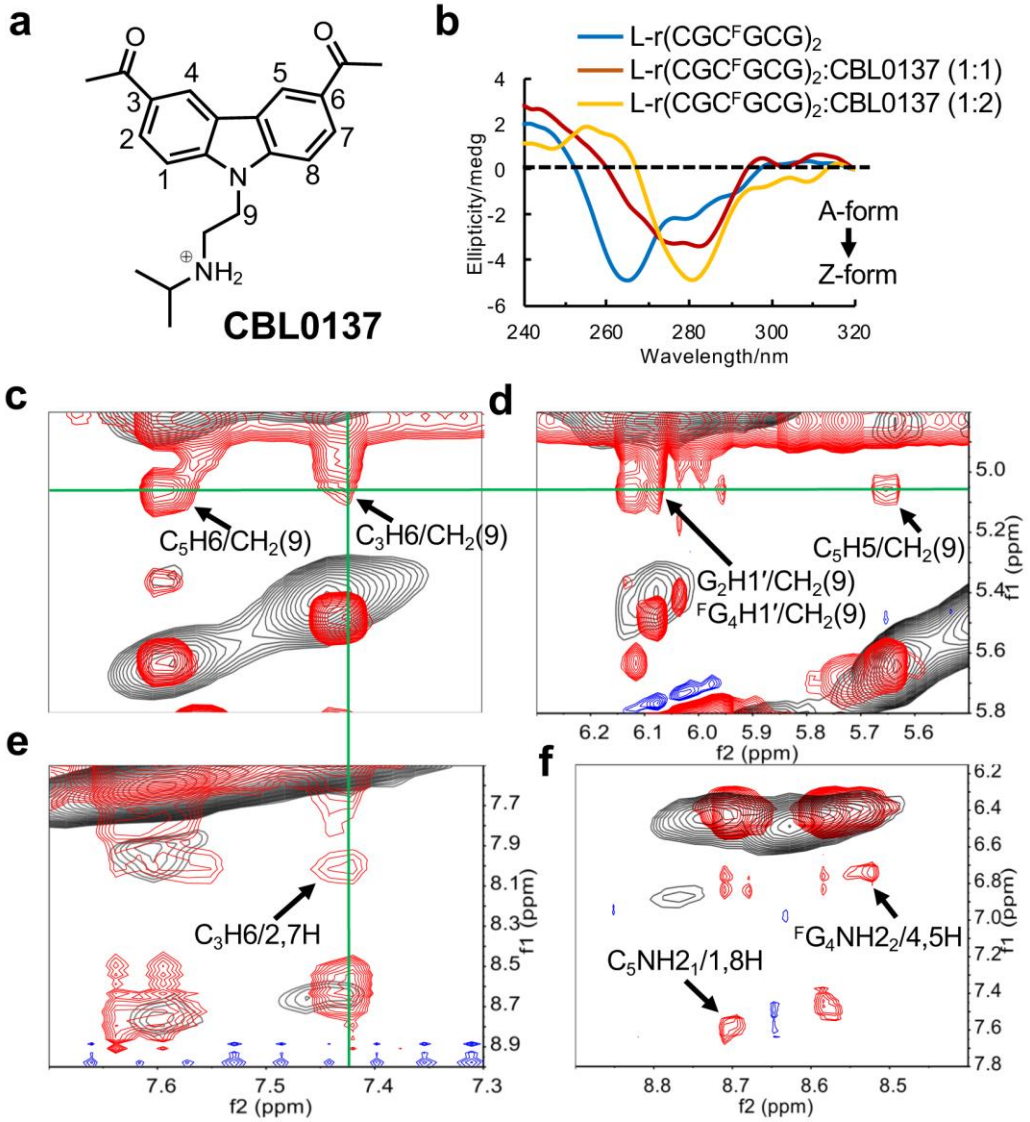

Figure 5. Study of CBL0137 ligand binding to Z-form RNA. (a) Structure of CBL0137, comprising a carbazole moiety with a positive charged N-side chain. (b) CD titration of Z-form RNA r(CGC^{F}GCG)$_2$ with increasing concentrations of CBL0137 at 10 °C in 5 mM Na-PO$_4$ buffer (pH 7.0). Ratio of CBL0137 to RNA is indicated on the top. (c-f) The overlay of NOE spectra. The signals in red from the complex CBL0137 and RNA. The signals in black from Z-form RNA as control. (c), (d) and (e) displays strong intermolecular NOEs between RNA and CBL0137. C$_5$H6/CH$_2$(9), C$_3$H6/CH$_2$(9), G$_2$H1′/CH$_2$(9), ^{F}G$_4$H1′/CH$_2$(9), C$_5$H5/CH$_2$(9) and C$_3$H6/2,7H marked by black arrows. The signals derived from CH$_2$(9) or C$_3$H6 were connected by green lines. (f) Black arrows indicated the NOEs between amino protons C$_5$NH2$_1$ and the aromatic protons (1H, 8H) of CBL0137, and the NOEs between amino protons ^{F}G$_4$NH2$_2$ and the aromatic protons (4H, 5H) of CBL0137.

Furthermore, to resolve the complex structure, 1D proton NMR experiments were constructed. As an increasing amount of CBL0137 was titrated into RNA, we observed the emergence of a new set

 doi:10.20944/preprints202410.0457.v1

of peaks for the complex after the titration (Supplemental Figure S7). This indicated that the binding of CBL0137 to RNA can be observed in a slow exchange regime on the NMR time-scale. The complete lists of ^{1}H chemical shifts of complex CBL0137 and RNA were shown in Supplemental Tables S3, S4 and S5. As the NMR signals preferred to be stable after the addition of double concentrations of CBL0137 into RNA, we deduced that only a dominant conformation of the 1:2 RNA-ligand complex was present. This is consistent with observations from CD titration experiments, which showed a clear inflection point around 1:2 for the complex formation (Supplemental Figure S8). Moreover, we found that addition of the ligand induced only a single peak of phosphate in C_3 of the GpC step with lower intensity from ^{31}P NMR spectrum (Supplemental Figure S9), as well as a resonance shift of $^{F}G_4$ in ^{19}F NMR (Supplemental Figure S10).

The overlay of 2D spectra derived from the complex of CBL0137 and RNA allowed us to get more precise NOE interactions between RNA and ligand (Figure 5c-5f). For example, a series of cross peaks showed the strong intermolecular interactions between $CH_2(9)$ in ligand and aromatic protons such as C_5H6, C_3H6, and C_5H5, as well as the sugar G_2H1', $^{F}G_4H1'$ protons of RNA. Similarly, the NOEs between the aromatic protons of CBL0137 and the amino protons or aromatic protons of RNA were detected. These results suggested that the ligand may insert into G_2:C_5 and C_3:$^{F}G_4$ base pairs by stacking effect.

The solution structure of the CBL0137-RNA complex was computed using NMR restraints (Figure 6a and Supplemental Figure S11). Two ligands were observed to symmetrically insert into G_2:C_5 and C_3:$^{F}G_4$base pairs at GpC step through π-stacking. An expanded view shows clearly the π-π stacking interactions between carbazole moiety of CBL0137 and base pairs (Figure 6b and Supplemental Figure S12). The cationic side chain of the ligand approached the phosphate backbone of C_3 through intense electrostatic interaction between the positively charged nitrogen atom of the ligand and the negatively charged phosphate backbone of C_3 (Figure 6c), while the acetyl groups at the position of 3 and 7 of carbazole protruded into the major groove (Supplemental Figure S13). This is in agreement with the observed NOE cross peak between the phosphate of C_3 and hydrogen of CBL0137 isopropyl from ^{31}P-^{1}H HOESY (heteronuclear overhauser effect spectroscopy) NMR (Supplemental Figure S14).

We noted that π-π stacking between planar carbazole moiety and base pairs of RNA produces a hydrophobic cavity as a cleft pocket in RNA (Figure 6d and Supplemental Figure S15). This suggests that the CBL0137 binding to Z-form RNA may result from a preference that Z-form RNA provides such a cleft pocket, whereas A-form RNA lacks the space for CBL0137 binding. This is consistent with a higher binding constant $K = 1.63 \times 10^5\ M^{-1}$ of CBL0137 and right-handed Z-form RNA $r(CGC^{F}GCG)_2$ complex compared to that of $K = 4.31 \times 10^4\ M^{-1}$ of CBL0137 and right-handed A-form RNA $r(CGCGCG)_2$ complex (Supplemental Figure S16).

 doi:10.20944/preprints202410.0457.v1

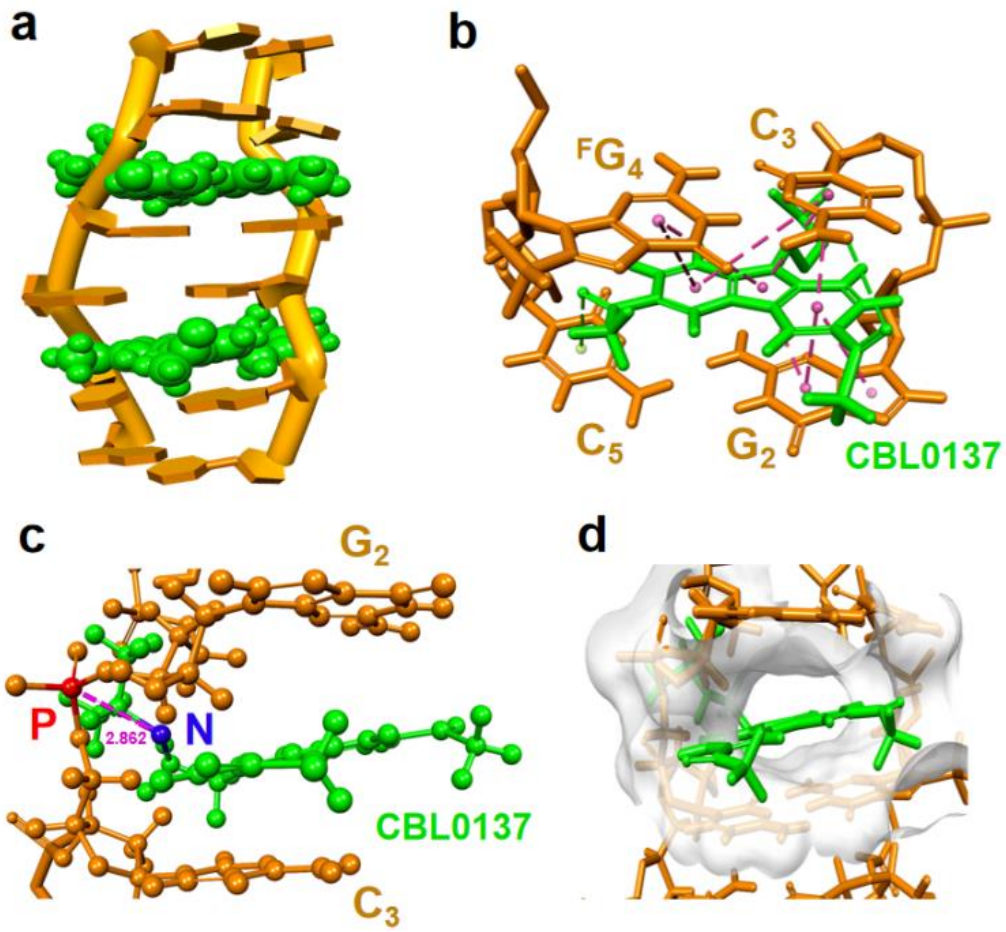

Figure 6. Molecular dynamic model of CBL0137 ligand binding to Z-form RNA in right-hand. (a) Solution structure of the CBL0137-RNA complex with cartoon representation. CBL0137 (in green CPK representation) symmetrically binding with Z-form RNA (orange) in 2:1 molecular ratio. (b) An expanded view of CBL0137 (in green stick representation) and base pairs indicated π-π stacking formation between carbazole moiety and base pairs of G_2:C_5 and C_3:$^FG_4$ as pink dashed lines connected by each aromatic rings center. (c) Side view showing the close proximity between the cationic N-side chain (shown as blue sphere) of CBL0137 and the anionic phosphate group (shown as red sphere) of C_3 (~2.862 Å in distance). (d) Solvent hydrophobicity surface of RNA (white) representation shows CBL0137 (in green stick representation) positioned in the cleft pocket.

3. Discussion

The present data clearly show the right-handed Z-form L-RNA are the exact mirror images of that of left-handed helix Z-form D-RNA, except for chirality both possess the same conformation. Such a fine structure provides an essential piece of information in the higher order structures of RNAs, completing the puzzle of mirror images of RNA A-form and Z-form enantiomers.

We demonstrated that curaxin CBL0137 interacts with right-handed Z-form RNA predominantly through π-stacking and electrostatic interactions. The conjugated aromatic ring of CBL0137 adopts a centrosymmetric orientation, facilitating π-π stacking interactions with the base pairs of the upper G2 and lower C3. However, the N-side chain of CBL0137 does not localize symmetrically but shifts towards the phosphate backbone of the C3 residue. This shift enables strong electrostatic interactions between the positively charged nitrogen of CBL0137 and the negatively charged phosphate backbone of C3 [27]. From the resolved structure of the complex, we infer that enhancing the binding affinity or selectivity of small molecules towards specific Z-form RNA structures can be achieved by optimizing the steric properties of the planar stacking and the cationic properties of the side chain.

 doi:10.20944/preprints202410.0457.v1

Previously study indicated that the Z-form DNA comprising 2′-deoxy-L-ribose adopt right-hand helix and could bind with small molecule [28,29]. These results collaborated with the findings in this study, are perfectly in line with our recent report, which displayed that CBL0137 triggers Z-form formation and contribute to its antitumor effects. Advanced NMR studies on the resulting complex of left-handed helix Z-form D-RNA and CBL0137 and the implications of their formation are currently underway.

4. Materials and Methods

4.1. RNA Sample Preparation

By using an automatic solid-phase phosphoramidite chemistry and DNA/RNA synthesizer, the D-, L-, and trifluoromethyl- labeled RNAs were synthesized at a ratio of 1.0 μmol. Following the RNAs were cleavage from the column and deprotected by using Ammonium Hydroxide/40% aqueous methylamine 1:1 v/v (AMA) at room temperature for 20 min and at 65 °C for 10 min, respectively. Tert-butyldimethylsilyl (TBDMS) protections were removed by treatment with triethylamine trihydrofluoride followed by filtration through an ion exchange cartridge. The oligomers were further purified by high performance liquid chromatography (HPLC) in a linear gradient of 50 mM ammonium formate in 1:1 acetonitrile/H_2O and 50 mM ammonium formate in H_2O. The oligomers were desalted through a NAP 10 column (disposable column, GE Healthcare) and identified by matrix-assisted laser desorption/ionization time-of-flight mass spectrometry (MALDI-TOF-MS) on an Autoflex III smart beam mass spectrometer (negative mode) (Supplemental Data S21-S24).

4.2. Circular Dichroism

CD experiments were performed by using a JASCO model J-820 CD spectrophotometer (JASCO Corporation, Tokyo, Japan). The RNA samples were prepared at a 10 μM concentration in the presence of different concentration of $NaClO_4$, and 5 mM Na-PO_4 buffer (pH7.0). For the CBL0137 and RNAs binding assay, RNAs were prepared at 10 μM in 5 mM $NaPO_4$ buffer (pH 7.0). CBL0137 was added into the RNA solution and kept at room temperature for 30 min before measurement. Titrating concentrations for ligands were prepared at ratios of [RNA duplex]/[CBL0137] as 1:0, 1:1 and 1:2 in the presence of fixed concentration (5 μM) of the duplex RNA. The binding constant K was calculated by analyzing CD data at a fixed wavelength versus ligand concentration according to previous study [30].

4.3. ^1H NMR Experiments

NMR data were recorded on a BRUKER AVANCE 400 and 600 MHz spectrometer. For spectra recorded in 90% H_2O/10% D_2O water signal was suppressed using the 3–9–19 WATER-GATE (water suppression by gradient tailored excitation) pulse sequence or excitation sculpting with gradient pulse. The data were processed with TopSpin 3.0 (Bruker BioSpin Gmbh) software and analyzed with MestReNova software. For 1D NMR measurement (^1H and ^{31}P spectrum), RNA samples of 0.3 or 2 mM concentration were dissolved in 150 μL of designed solution containing 10% D_2O, 2 M $NaClO_4$ and 10 mM Na-PO_4 buffer (pH 7.0). Two-dimensional NOESY spectra in 90% H_2O/10% D_2O was collected from 512 scans with 400 ms mixing time at 20 °C. On average, 2048 complex points and 512 FIDs (free induction decay) were collected within the spectral width of 14097 Hz. The sample solutions were as follows: 2 mM RNA were dissolved in 150 μL of designed solution containing 10% D_2O, 2 M $NaClO_4$ and 10 mM Na-PO_4 buffer (pH 7.0). Heteronuclear 2D NOESY spectra (^1H–^{31}P) was carried out in identical solution containing 10% D_2O, 2 M $NaClO_4$ and 10 mM Na-PO_4 buffer (pH 7.0), in which the chemical shift of phosphate from Na-PO_4 was referred as internal standard at 0 ppm. Samples were prepared by heating the oligonucleotides at 85 °C for 3 min and gradually cooling to room temperature. For studying the RNA duplex binding with CBL0137 ligand, the samples were prepared by denaturing and annealing of RNA and followed by incubating at 4 °C overnight before

 doi:10.20944/preprints202410.0457.v1

additional ligand. Condition: 0.15 or 1 mM RNA duplex with 0.3 or 2 mM CBL0137 dissolved in the solution of 2 M $NaClO_4$ and 10 mM Na-PO_4 buffer (pH 7.0) containing 10% D_2O.

4.4. ^{19}F NMR Experiments

For ^{19}F NMR measurement, RNA samples of 100 μM concentration were dissolved in 150 μL of designed solution containing 10% D_2O, in the presence of different concentration of $NaClO_4$ and 5 mM Na-PO_4 buffer (pH 7.0). Samples were prepared by heating the ^{19}F-labeled oligonucleotides at 90 °C for 3 minutes and gradually cooling to room temperature. The ^{19}F NMR spectrum was measured on a Bruker AVANCE 400 MHz spectrometer at a frequency of 376.05 MHz and referenced to the internal standard CF_3COOH (–75.66 ppm). The experimental parameters are recorded as follows: spectral width 89.3 kHz, ^{19}F excitation pulse 15.0 μs, relaxation delay 1.5 s, acquisition time 0.73 s, scan numbers 1000, temperature 10 °C.

4.5. Structural Determination

All assigned NOESY cross peaks were classified to strong (1.8-3.0 Å), medium (3.0-3.7 Å), weak (3.7-5.5 Å) and very weak (5.5-7.5 Å) inter-proton distance restraints based on the intensity of NOESY. The NOE peaks of H5-H6 from cytosine bases were used as calibration for the distance measurements. Distance restraints for the hydrogen bonding in each Watson-Crick base pair were 1.8-3.7 Å. The force constant of hydrogen bonds and NOE restraints were kept between 5 to 50 kcal mol^{-1} $Å^{-2}$ throughout the computation. Then molecular dynamics simulations were performed by the structural solvation and standard dynamics cascade in BIOVIA Discovery Studio 4.5 with modifications. Generally, the structure was heating from 50 K to 300 K over 4ps and equilibration at 300 K with 100 ps simulation time. The save results interval in the production step was 2ps during 100 ps simulation time at 300 K. 10 best conformations generated by simulation were further energy minimized until the gradient of energy was less than 0.1 kcal mol^{-1}. The conformation with lowest energy was selected as the final presentation. The all-atom RMSD were calculated using Z-form L-RNA in superimposition.

4.6. Molecular Modeling

We manually prepared the initial model using L-ribonucleosides, which are the mirror images of D-ribonucleosides, while following the structural features of known Z-form D-RNA and D-DNA. The L-RNA model (PDB: 1R3O) served as the template for this preparation. by Above all molecular model construction accomplished by BIOVIA Discovery Studio 4.5.

4.7. Molecular Docking Simulation

The molecular docking calculations were performed by using the BIOVIA Discovery Studio 4.5. All assigned NOESY cross peaks in the Z-form L-RNA duplex/CBL0137 complex were used to determine the inter-proton distance restraints. The NOE peaks of H5-H6 from cytosine bases were used as calibration for the distance measurements. The structure of CBL0137 was optimized before use as a ligand in the binding assay. Z-form L-RNA duplex was collected from the former NMR structure in solution in this study. All possible docking sites were provided by the BIOVIA Discovery Studio 4.5 based on calculation results and further selected reasonably according to the NOEs intensities. The docking experiment was implemented and provided at least 5 conformations, in which the proper one was used to the next standard dynamics cascade and energy minimization processes. Total 5 conformations were generated and the conformation with lowest energy was selected as the final presentation. The all-atom RMSD were calculated using Z-form L-RNA-CBL0137 complex in superimposition.

5. Conclusions

 doi:10.20944/preprints202410.0457.v1

In summary, we described the first observation of a right-handed Z-form L-RNA at first time, and demonstrated its binding with CBL0137 ligand at high resolution. These results indicated that the new nucleic acid structure might produce applicable biofunctions.

Supplementary Materials: The following supporting information can be downloaded at the website of this paper posted on Preprints.org., Figure S1: Anomeric regions of Z-form RNA in 2D NOESY; Figure S2: Structural model of Z-form RNA L-r(CGC^{F}GCG)$_2$; Figure S3: Inter-strand Watson-Crick base pairs involved in the Z-form RNA duplex; Figure S4: Stick model of Z-form RNA; Figure S5: Stacking pattern within the CpG and GpC steps in Z-form RNA as viewed along the helix z-axis; Figure S6: The refined structure of Z-form RNA L-r(C$_1$G$_2$C$_3$^{F}G$_4$C$_5$G$_6$)$_2$ is a half turn of a right-handed RNA helix; Figure S7: 1D NMR spectra of Z-form L-r(CGC^{F}GCG)$_2$ with CBL0137; Figure S8: Study of CBL0137 ligand binding to Z-form RNA; Figure S9: ^{31}P spectra of Z-form L-r(CGC^{F}GCG)$_2$/CBL0137 complex; Figure S10: ^{19}F spectra of Z-form L-r(CGC^{F}GCG)$_2$/CBL0137 complex; Figure S11: Structural model of Z-form RNA L-r(CGC^{F}GCG)$_2$ and CBL0137 complex; Figure S12: An expanded view of RNA and CBL0137 complex model; Figure S13: Molecular model show the acetyl groups (purple, CPK presentation) at the position of 3 and 7 of carbazole (green, CPK presentation) protruded into the major groove of Z-form duplex; Figure S14: 2D heteronuclear ^{31}P-^{1}H NMR spectroscopy of Z-form RNA L-r(CGC^{F}GCG)$_2$ and CBL0137 complex; Figure S15: Molecular model of Z-form L-r(CGC^{F}GCG)$_2$/CBL0137 complex; Figure S16: Titration data of CBL0137 and RNA derived by monitoring the wavelength at 280 nm of CD. Figure S17-S36: synthesis of 8-^{F}G-modified L-guanosine phosphoramidite; Figure S37-S40: MALDI-MS of oligonucleotide in this study; Table S1: ^{1}H chemical shift assignments of Z-form RNA L-r(CGC^{F}GCG)$_2$; Table S2: ^{1}H chemical shift assignments of CBL0137; Table S3: ^{1}H chemical shift assignments of Z-form RNA L-r(CGC^{F}GCG)$_2$ in presence of CBL0137; Table S4: ^{1}H chemical shift assignments of CBL0137 in presence of Z-form RNA L-r(CGC^{F}GCG)$_2$.

Author Contributions: The two authors contributed equally: Yi Song, Shiyu Wang. All authors have given approval to the final version of the manuscript.

Funding: This work was supported by JSPS KAKENHI Grant Numbers 21H02081 (to Y.X.) and 24K01648 (to Y.X.).

Institutional Review Board Statement: Not applicable.

Informed Consent Statement: Not applicable.

Data Availability Statement: The raw data supporting the conclusions of this article will be made available by the authors upon request.

Conflicts of Interest: The authors declare no conflicts of interest.

References

1. Wan, Y.; Kertesz, M.; Spitale, R. C.; Segal, E.; Chang, H. Y. Understanding the transcriptome through RNA structure. *Nat. Rev. Genet.* **2011,** *12*, 641-655. [CrossRef] [PubMed]
2. Dong, T.; Wang, M.; Liu, J.; Ma, P.; Pang, S.; Liu, W.; Liu, A. Diagnostics and analysis of SARS-CoV-2: current status, recent advances, challenges and perspectives. *Chem. Sci.* **2023,** *14*, 6149-6206. [CrossRef] [PubMed]
3. Zhang, T.; Yin, C.; Boyd, D. F.; Quarato, G.; Ingram, J. P.; Shubina, M.; Ragan, K. B.; Ishizuka, T.; Crawford, J. C.; Tummers, B.; et al. Influenza virus Z-RNAs induce ZBP1-mediated necroptosis. *Cell* **2020,** *180*, 1115-1129. [CrossRef] [PubMed]
4. Ji, D.; Lyu, K.; Zhao, H.; Kwok, C. K. Circular L-RNA aptamer promotes target recognition and controls gene activity. *Nucleic Acids Res.* **2021,** *49*, 7280-7291. [CrossRef] [PubMed]
5. Umar, M. I.; Chan, C.-Y.; Kwok, C. K. Development of RNA G-quadruplex (rG4)-targeting l-RNA aptamers by rG4-SELEX. *Nat. Protoc.* **2022,** *17*, 1385-1414. [CrossRef] [PubMed]
6. Pu, F.; Ren, J.; Qu, X. Nucleobases, nucleosides, and nucleotides: versatile biomolecules for generating functional nanomaterials. *Chem. Soc. Rev.* **2018,** *47*, 1285-1306. [CrossRef] [PubMed]
7. Oberthür, D.; Achenbach, J.; Gabdulkhakov, A.; Buchner, K.; Maasch, C.; Falke, S.; Rehders, D.; Klussmann, S.; Betzel, C. Crystal structure of a mirror-image L-RNA aptamer (Spiegelmer) in complex with the natural L-protein target CCL2. *Nat. Commun.* **2015,** *6*, 6923. [CrossRef] [PubMed]
8. Ji, D.; Yuan, J.-H.; Chen, S.-B.; Tan, J.-H.; Kwok, C. K. Selective targeting of parallel G-quadruplex structure using L-RNA aptamer. *Nucleic Acids Res.* **2023,** *51*, 11439-11452. [CrossRef] [PubMed]
9. Dey, S.; Sczepanski, J. T. In vitro selection of l-DNA aptamers that bind a structured d-RNA molecule. *Nucleic Acids Res.* **2020,** *48*, 1669-1680. [CrossRef] [PubMed]
10. Umar, M. I.; Kwok, C. K. Specific suppression of D-RNA G-quadruplex–protein interaction with an L-RNA aptamer. *Nucleic Acids Res.* **2020,** *48*, 10125-10141. [CrossRef] [PubMed]

11. Zhou, L.-Y.; Qin, Z.; Zhu, Y.-H.; He, Z.-Y.; Xu, T. Current RNA-based therapeutics in clinical trials. *Curr. Gene Ther.* **2019,** *19*, 172-196. [CrossRef] [PubMed]
12. Skaanning, M. K.; Bønnelykke, J.; Nijenhuis, M. A.; Samanta, A.; Smidt, J. M.; Gothelf, K. V. Self-Assembly of Ultrasmall 3D Architectures of (l)-Acyclic Threoninol Nucleic Acids with High Thermal and Serum Stability. *J. Am. Chem. Soc.* **2024,** *146*, 20141-20146. [CrossRef] [PubMed]
13. Herbert, A. Z-DNA and Z-RNA in human disease. *Commun. Biol.* **2019,** *2*, 7. [CrossRef] [PubMed]
14. Jiao, H.; Wachsmuth, L.; Kumari, S.; Schwarzer, R.; Lin, J.; Eren, R. O.; Fisher, A.; Lane, R.; Young, G. R.; Kassiotis, G.; et al. Z-nucleic-acid sensing triggers ZBP1-dependent necroptosis and inflammation. *Nature* **2020,** *580*, 391-395. [CrossRef] [PubMed]
15. Mondal, M.; Yang, L.; Cai, Z.; Patra, P.; Gao, Y. Q. perspective on the molecular simulation of DNA from structural and functional aspects. *Chem. Sci.* **2021,** *12*, 5390-5409. [CrossRef] [PubMed]
16. Ha, S. C.; Lowenhaupt, K.; Rich, A.; Kim, Y.-G.; Kim, K. K. Crystal structure of a junction between B-DNA and Z-DNA reveals two extruded bases. *Nature* **2005,** *437*, 1183-1186. [CrossRef] [PubMed]
17. Zhang, T.; Yin, C.; Fedorov, A.; Qiao, L.; Bao, H.; Beknazarov, N.; Wang, S.; Gautam, A.; Williams, R. M.; Crawford, J. C.; et al. ADAR1 masks the cancer immunotherapeutic promise of ZBP1-driven necroptosis. *Nature* **2022,** *606*, 594-602. [CrossRef] [PubMed]
18. Hubbard, N. W.; Ames, J. M.; Maurano, M.; Chu, L. H.; Somfleth, K. Y.; Gokhale, N. S.; Werner, M.; Snyder, J. M.; Lichauco, K.; Savan, R.; et al. ADAR1 mutation causes ZBP1-dependent immunopathology. *Nature* **2022**, 607, 769-775. [CrossRef] [PubMed]
19. Hall, K.; Cruz, P.; Tinoco Jr, I.; Jovin, T. M.; Van De Sande, J. H. 'Z-RNA'—a left-handed RNA double helix. *Nature* **1984,** *311*, 584-586. [CrossRef]
20. Balasubramaniyam, T.; Ishizuka, T.; Xiao, C.-D.; Bao, H.-L.; Xu, Y. 2′-O-Methyl-8-methylguanosine as a Z-Form RNA Stabilizer for Structural and Functional Study of Z-RNA. *Molecules* **2018,** *23*, 2572. [CrossRef] [PubMed]
21. Nichols, P. J.; Krall, J. B.; Henen, M. A.; Welty, R.; Macfadden, A.; Vicens, Q.; Vögeli, B. Z-Form Adoption of Nucleic Acid is a Multi-Step Process Which Proceeds through a Melted Intermediate. *J. Am. Chem. Soc.* **2023,** *146*, 677-694. [CrossRef] [PubMed]
22. Xu, Y.; Ikeda, R.; Sugiyama, H. 8-Methylguanosine: a powerful Z-DNA stabilizer. *J. Am. Chem. Soc.* **2003,** *125*, 13519-13524. [CrossRef] [PubMed]
23. Bao, H.-L.; Masuzawa, T.; Oyoshi, T.; Xu, Y. Oligonucleotides DNA containing 8-trifluoromethyl-2′-deoxyguanosine for observing Z-DNA structure. *Nucleic Acids Res.* **2020,** *48*, 7041-7051. [CrossRef] [PubMed]
24. Xu, Y.; Zhang, Y. X.; Sugiyama, H.; Umano, T.; Osuga, H.; Tanaka, K. (P)-helicene displays chiral selection in binding to Z-DNA. *J. Am. Chem. Soc.* **2004,** *126*, 6566-6567. [CrossRef] [PubMed]
25. Wang, S.; Xu, Y. RNA structure promotes liquid-to-solid phase transition of short RNAs in neuronal dysfunction. *Commun. Biol.* **2024,** *7*, 137. [CrossRef] [PubMed]
26. Bao, H.-L.; Xu, Y. Investigation of higher-order RNA G-quadruplex structures in vitro and in living cells by ^{19}F NMR spectroscopy. *Nat Protoc.* **2018,** *13*, 652-665. [CrossRef] [PubMed]
27. Dallavalle, S.; Mattio, L. M.; Artali, R.; Musso, L.; Aviñó, A.; Fàbrega, C.; Eritja, R.; Gargallo, R.; Mazzini, S. Exploring the interaction of curaxin CBL0137 with G-quadruplex DNA oligomers. *Int. J. Mol. Sci.* **2021,** *22*, 6476. [CrossRef] [PubMed]
28. Drozdzal, P., Manszewski, T., Gilski, M., Brzezinski, K. and Jaskolski, M. (2023) Right-handed Z-DNA at ultrahigh resolution: a tale of two hands and the power of the crystallographic method. *Acta Crystallogr. D Struct. Biol.*, **79**, 133-139. [CrossRef] [PubMed]
29. Urata, H., Ogura, E., Shinohara, K., Ueda, Y. and Akagi, M. (1992) Synthesis and properties of mirror-image DNA. *Nucleic Acids Res.*, **1992**, 20, 3325-3332. [CrossRef] [PubMed]
30. Stootman, F. H.; Fisher, D. M.; Rodger, A.; Aldrich-Wright, J. R. Improved curve fitting procedures to determine equilibrium binding constants. *Analyst* **2006,** *131*, 1145-1151. [CrossRef] [PubMed]